We are IntechOpen, the world's leading publisher of Open Access books Built by scientists, for scientists

6,900
Open access books available

185,000
International authors and editors

200M
Downloads

Our authors are among the

154
Countries delivered to

TOP 1%
most cited scientists

12.2%
Contributors from top 500 universities



WEB OF SCIENCE™

Selection of our books indexed in the Book Citation Index in Web of Science™ Core Collection (BKCI)

Interested in publishing with us?
Contact book.department@intechopen.com

Numbers displayed above are based on latest data collected.
For more information visit www.intechopen.com



Chapter

Thermal Collective Excitations in Novel Two-Dimensional Dirac-Cone Materials

Andrii Iurov, Godfrey Gumbs and Danhong Huang

Abstract

The purpose of this chapter is to review some important, recent theoretical discoveries regarding the effect of temperature on the property of plasmons. These include their dispersion relations and Landau damping rates, and the explicit dependence of plasmon frequency on chemical potential at finite temperatures for a diverse group of recently discovered Dirac-cone materials. These novel materials cover gapped graphene, buckled howycomb lattices (such as silicene and germanene), molybdenum disulfide and other transition-metal dichalcogenides, especially the newest dice and α-$\mathcal{T}_3$ materials. The most crucial part of this review is a set of implicit analytical expressions about the exact chemical potential for each of considered materials, which greatly affects the plasmon dispersions and a lot of many-body quantum-statistical properties. We have also obtained the nonlocal plasmon modes of graphene which are further Coulomb-coupled to the surface of a thick conducting substrate, while the whole system is kept at a finite temperature. An especially rich physics feature is found for α-$\mathcal{T}_3$ materials, where each of the above-mentioned properties depends on both the hopping parameter α and temperature as well.

Keywords: finite temperature effects, plasmon dispersion, 2D materials

1. Introduction

Graphene, a two-dimensional (2D) carbon layer with a hexagonal atomic structure [1–3], has recently attracted outstanding attention from both academic scientists doing fundamental researches and engineers working on its technical applications [4]. Now, the scientific community is actively investigating the innovative semiconductors beyond graphene, with intrinsic spin-orbit interaction and tunable bandgap [5].

A remarkable feature of graphene is the absence of the bandgap in its energy dispersions. In spite of the obvious advantage of such bandstructure for novel electronic devices, electrons in graphene could not be confined due to the well-known Klein paradox [6]. To resolve this issue, graphene may be replaced with a material with a buckled structure and substantial spin-orbit interaction, such as silicene and germanene.

A new quasi-two-dimensional structure which has recently gained popularity among device scientists, is molybdenum disulfide monolayer, a honeycomb lattice

which consists of two different molybdenum and sulfur atoms. It reveals a large direct band gap, absence of inversion symmetry and a substantial spin-orbit coupling. A summary of all recently fabricated materials beyond graphene is given in **Figure 1**. The last relevant example is black phosphorous (phosphorene) with a strong anisotropy of its composition and electron energy dispersion. Even though we do not study plasmons in phosphorene in the present chapter, there have been some crucial publications on that subject [7, 8].

Plasmons, or self-sustained collective excitations of interacting electrons in such low-dimensional materials, are especially important, since they serve as the basics for a number of novel devices and their applications [9, 10] in almost all fields of modern science, emerging nanofabrication and nanotechnology. Propagation and detection of plasmonic excitation in hybrid nanoscale devices can convert to or modify existing electromagnetic field or radiation [11–14]. Localized surface plasmons are particularly of special interest considering their interactions with other plasmon modes in closely-located optoelectronic device as well as with imposed electromagnetic radiation [15].

Finite-temperature plasmons are of special interest for possible device applications. Among them is the possibility to increase the frequency (or energy) of a plasmon by an order of magnitude or even more, specifically, as a consequence of the raised temperature. As it was shown in Ref. [16], the dispersion of a thermal plasmon is given as $\sim \sqrt{q k_B T}$, where q is the wave vector. This dispersion relation reveals the fact that the plasmon energy is monotonically increased with temperature and could be moved to the terahertz range and even above, which is crucial for imaging and spectroscopy.

At the same time, the damping rate, or broadening of the frequency, of such thermal plasmons varies as $\simeq 1/\sqrt{T}$, which means that we are dealing with a long-lived plasmon with low or even nearly zero Landau damping. Both plasmon

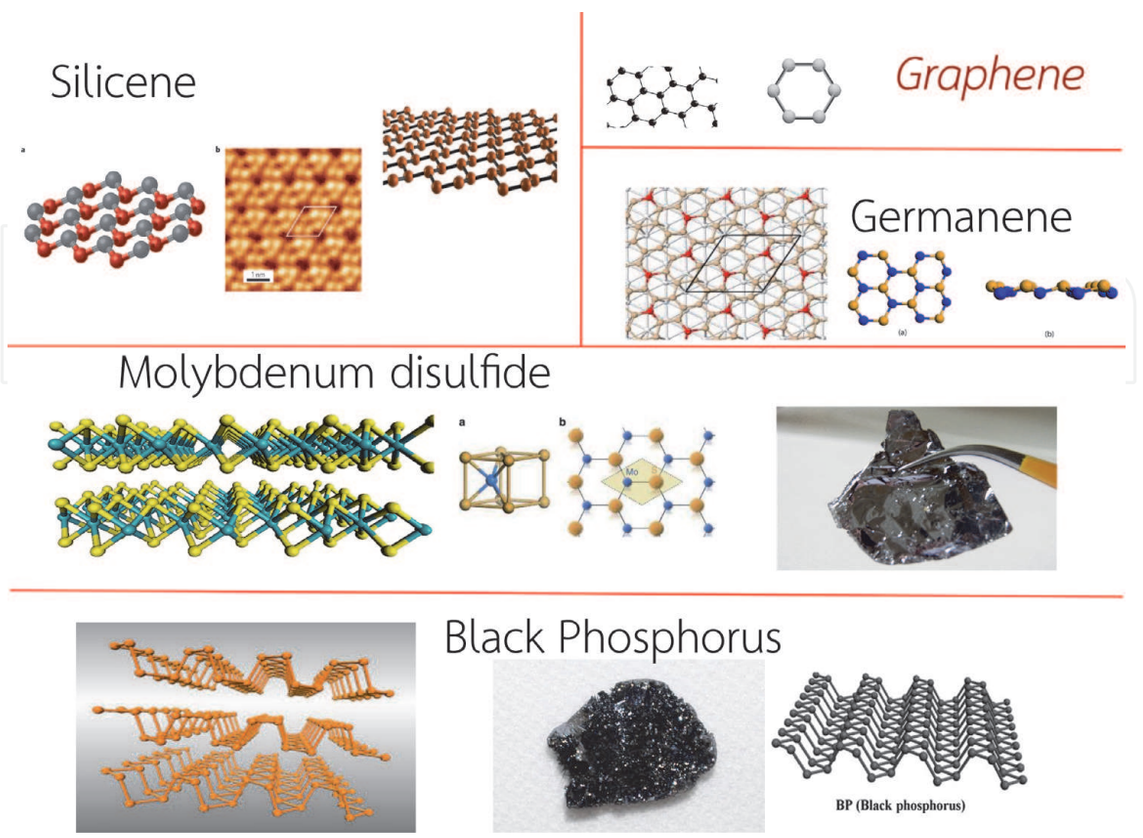


Figure 1.
Recently discovered two-dimensional materials: graphene and beyond graphene.

frequency and the corresponding damping rate at finite temperature could be adjusted by electron doping, and could also be determined for an intrinsic material, where the chemical potential at $T = 0K$ is located exactly at the Dirac point, while for zero temperature, intrinsic plasmons in graphene do not exist.

In this chapter, we will consider thermal behavior of plasmons, their dispersions and damping rates. By equipping with this information, it is possible to predict in advance the thermal properties of an electronic device designed for a particular temperature range. In spite of a number of reported theoretical studies on this subject [16–18], there is still a gap on demonstrating experimentally these unique thermal collective features of 2D materials. Therefore, our review can serve as an incentive to address this issue.

2. Novel two-dimensional materials beyond graphene

All the novel 2D materials considered here could be effectively assigned to an individual category based on their existing (or broken) symmetries and degeneracy in their low-energy band structure. We started with graphene having a bandgap Δ_0 and single-particle energy bands $\varepsilon_{\pm}(k) = \pm\sqrt{(\hbar v_F k)^2 + \Delta_0^2}$, which are symmetric with respect to the Dirac point. Moreover, there is a total spin-valley degeneracy $g = g_s g_v = 4$ for electrons and holes in each band.

Silicene and germanene, which represent buckled honeycomb lattices, possess subbands depending on valley and spin indices, and therefore are only doubly-degenerate. The electron-hole symmetry is broken for molybdenum disulfide and other transition-metal dichalcogenides (TMDC's). For these situations, even though there exists a single electron-hole index $\gamma = \pm 1$, the energy of corresponding states does not have opposite values for each wave number, even at the valley point. In contrast to the electron states, the hole subbands reveal a splitting, as shown in **Figure 2**. All these partially broken symmetries strongly affect the chemical potential of 2D materials as well as its finite-temperature many-body properties. Black phosphorous, apart from all previously discussed broken symmetries, further acquires a preferred spatial direction in its atomic structure which leads to a strong anisotropy of its electronic states and band structures.

2.1 Buckled honeycomb lattices

The energy dispersions of buckled honeycomb lattices, obtained from a Kane-Mele type Hamiltonian, appear as two inequivalent doubly-degenerate pairs of subbands with the same Fermi velocity $v_F = 0.5 \times 10^6$ m/s and are given by

$$\varepsilon^{\gamma}_{\xi,\sigma}(k) = \gamma\sqrt{(\xi\sigma\Delta_z - \Delta_{SO})^2 + (\hbar v_F k)^2}, \tag{1}$$

where $\gamma = \pm 1$ labels symmetric electron and hole states. Here, two bandgaps [19, 20] $\Delta_< = |\Delta_{SO} - \Delta_z|$ and $\Delta_> = \Delta_{SO} + \Delta_z$ are attributed to an intrinsic spin-orbit gap $\Delta_{SO} = 0.5 - 3.5$ meV [21–24] and a tunable asymmetry bandgap Δ_z proportional to applied electric field $\mathcal{E}_z$. The band structure, however, depends only on one composite index $\nu = \sigma\xi$, a product of spin σ and valley ξ index. At $\mathcal{E}_z = 0$, two gaps become the same. As $\mathcal{E}_z \neq 0$, $\Delta_<$ and $\Delta_>$ change in opposite ways, and electrons stay in a topological insulator (TI) state. Additionally, $\Delta_<$ decreases with $\mathcal{E}_z$ until reaching zero, corresponding to a new valley-spin polarized metal. On the other hand, if $\mathcal{E}_z$ further increases, both $\Delta_<$ and $\Delta_>$ will be enhanced, leading to a

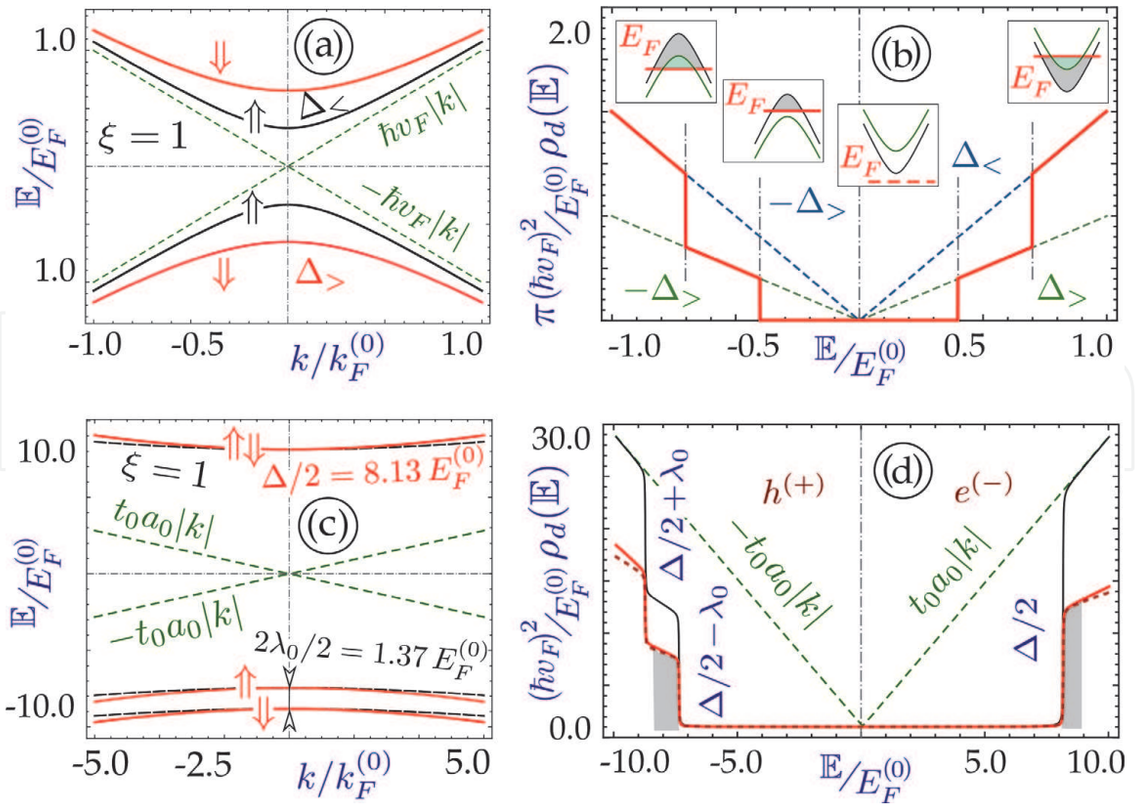


Figure 2.
Energy dispersions and density of states (DOS) $\rho_d(\mathbb{E})$ of silicene [(a) and (b)] and molybdenum disulfide MoS_2 [(c) and (d)], where $E_F^{(0)}$ and $k_F^{(0)}$ are Fermi energy and wave number, respectively. For MoS_2, its dispersions and DOS, corresponding to parabolic band approximation in Eq. (23), are also shown for comparison.

standard band insulator (BI) state for electrons. As we will see below, all of the single electronic and collective properties of buckled honeycomb lattices depend on both bandgaps $\Delta_{<,>}$, and therefore could be tuned by varying a perpendicular electric field to create various types of functional electronic devices.

The wave function of silicene, corresponding to eigenvalue equation in Eq. (1), takes the form [25]

$$\Psi^{\gamma}(k) = \begin{bmatrix} \Psi^{\gamma}_{\xi=1,\sigma=+1}(k) \\ \Psi^{\gamma}_{\xi=1,\sigma=-1}(k) \end{bmatrix},$$
$$\Psi^{\gamma}_{\xi,\sigma}(k) = \sqrt{\frac{\gamma}{2\varepsilon^{\gamma}_{\xi,\sigma}(k)}} \begin{bmatrix} \sqrt{|\varepsilon^{\gamma}_{\xi,\sigma}(k) + \Delta_0^{\xi,\sigma}|} \\ \gamma\sqrt{|\varepsilon^{\gamma}_{\xi,\sigma}(k) - \Delta_0^{\xi,\sigma}|}\, e^{i\theta_k} \end{bmatrix}, \tag{2}$$

where $\theta_k = \tan^{-1}(k_y/k_x)$ and $\Delta_0^{\xi,\sigma} = |\xi\sigma\Delta_z - \Delta_{SO}|$.

Germanene, another representative of buckled honeycomb lattices [26–30], demonstrates substantially higher Fermi velocities and an enhanced intrinsic bandgap ~ 23 meV. For a free-standing germanene, first-principles studies have revealed a buckling distances $\sim 0.640.74$ Å [31, 32].

2.2 Molybdenum disulfide and transition-metal dichalcogenides

MoS_2 is a typical representative of transition-metal dichalcogenide (TMDC) monolayers. TMDC's are semiconductors with the composition of TC_2 type, where

T refers to a transition-metal atom, such as Mo or W, while C corresponds to a chalcogen atom (S, Se or Te).

MoS_2 displays broken inversion symmetry and direct bandgaps. Its most crucial distinction from the discussed buckled honeycomb lattices is its broken symmetry between the electrons and holes so that the corresponding energy bands are no longer symmetric with respect to the Dirac point, but could still be classified by a single index $\gamma = \pm 1$. The absence of this particle-hole symmetry is expected to have a considerable effect on the plasmon branches at both zero and finite temperatures through the thermal convolution of the corresponding quantum states.

Specifically, the energy bands of MoS_2 can be described by a *two-band* model, i.e.,

$$\varepsilon_{\gamma}^{\xi,\sigma}(k) \simeq \frac{1}{2}\xi\sigma\lambda_0 + \frac{\alpha\hbar^2}{4m_e}k^2 + \frac{\gamma}{2}\sqrt{\left[(2t_0a_0)^2 + (\Delta - \xi\sigma\lambda_0)\beta\hbar^2/m_e\right]k^2 + (\Delta - \xi\sigma\lambda_0)^2}, \tag{3}$$

where $\Delta = 1.9$ eV is a gap parameter leading to an extremely large direct bandgap $\simeq 1.7$ eV. There is also substantial internal spin-orbit coupling $\lambda_0 = 0.042\,\Delta$, $t_0a_0 = 4.95 \times 10^{-29}$ J m is a Dirac-cone term, where $t_0 = 0.884\ \Delta$ is the electron hopping parameter while $a_0 = 1.843$ Å is the lattice constant. The t_0a_0 term is ≈ 0.47 compared to $\hbar v_F$ in graphene. Similarly to silicene and germanene, the energy dispersions of TMDC's depend on one composite valley-spin index $\nu = \sigma\xi$. There are also other less important but still non-negligible $\sim k^2$ mass terms with $\alpha = 2.21 = 5.140\beta$, and m_e represents the mass of a free electron.

In practical, we will neglect the $\simeq k^4$ terms, $\simeq t_1a_0^2$ trigonal warping term and anisotropy, which indeed have tiny or no effect on the density of states of the considered material, but would make our model much more complicated. The above dispersions could be presented in a form similarly to those for gapped graphene, i.e., $\varepsilon_{\gamma}^{\nu}(k) = \mathbb{E}_0^{\nu}(k) + \gamma\sqrt{\left[\Delta_0^{\nu}(k)\right]^2 + (t_0a_0k)^2}$, where $\Delta_0^{\nu}(k) = \hbar^2k^2\beta/4m_e + \Delta/2 - \nu\lambda_0/2$ is a k-dependent "gap term" and the band shift is $\mathbb{E}_0^{\nu}(k) = \hbar^2k^2\alpha/4m_e + \nu\lambda_0/2$. A set of somewhat cumbersome analytical expressions for the components of the wave functions corresponding to dispersions in Eq. (3) can be found from Ref. [25].

Using Eq. (3), we can verify that the degeneracy of two hole subbands ($\gamma = -1$), corresponding to $\nu = \pm 1$, will be lifted and two subband will be separated by $\lambda_0 \simeq 79.8$ meV. However, this is not the case for two corresponding electron states ($\gamma = 1$). Consequently, the electron-hole asymmetry exists even at $k = 0$ and becomes even more pronounced at finite k values. One can clearly see this difference by comparing **Figure 2(b)** with **Figure 2(d)**.

3. Thermal plasmons in graphene and other materials

One of the most important features in connection with plasmons at zero and finite temperatures is its dispersion relations, i.e., dependence of the plasmon frequency ω on wave number q. Physically, these complex relations can be determined from the zeros of a dielectric function $\epsilon_T(q,\omega)$, [19, 33] given by

$$\epsilon_T(q,\omega) = 1 - v(q)\,\Pi_T(q,\omega|\mu(T)) = 0, \tag{4}$$

where $v(q) = 2\pi\alpha_r/q \equiv e^2/2\epsilon_0\epsilon_r q$ is the 2D Fourier-transformed Coulomb potential, $\alpha_r = e^2/4\pi\epsilon_0\epsilon_r$, and ϵ_r represents the dielectric constant of the host material.

The dielectric function introduced in Eq. (4) is determined directly by the finite-temperature *polarization function*, or *polarizability*, $\Pi_T(q,\omega\,|\,\mu(T))$, which is,

in turn, related to its *zero-temperature counterpart*, $\Pi_0(q,\omega\,|E_F)$, by an integral convolution with respect to different Fermi energies [34], given by

$$\Pi_T(q,\omega\,|\,\mu(T)) = \frac{1}{2k_BT}\int_0^\infty d\eta\,\frac{\Pi_0(q,\omega\,|\,\eta)}{1+\,\cosh\left[(\mu-\eta)/k_BT\right]}, \tag{5}$$

where the integration variable η stands for the electron Fermi energy at $T=0$. This equation is derived for electron doping with $\eta = E_F > 0$. We note that, in order to evaluate this integral, one needs to know in advance how the chemical potential $\mu(T)$ varies with temperature T. Such a unique T dependence reflects a specific selection of a convolution path for a particular material band structure, which we will discuss in Section 4.

The zero-temperature polarizability, which is employed in Eq. (5), is quite similar for all 2D materials considered here. The only difference originates from the degeneracy level of the low-energy band structure, such as $g = g_v g_s = 4$ for graphene with either finite or zero bandgap. We begin with the expression of the partial polarization function with two inequivalent doubly-degenerate pairs of subbands labeled by a composite index ν

$$\begin{aligned}\Pi_0^{(\nu)}(q,\omega\,|\,E_F) = \frac{1}{4\pi^2}\int d^2\boldsymbol{k}\sum_{\gamma,\gamma'=\pm1}\left\{1+\gamma\gamma'\,\frac{\boldsymbol{k}\cdot(\boldsymbol{k}+\boldsymbol{q})+\Delta_\nu^2}{\varepsilon_\gamma^\nu(k)\,\varepsilon_{\gamma'}^\nu(|\boldsymbol{k}+\boldsymbol{q}|)}\right\}\\ \times\frac{\Theta_0\left[E_F-\varepsilon_\gamma^\nu(k)\right]-\Theta_0\left[E_F-\varepsilon_{\gamma'}^\nu(|\boldsymbol{k}+\boldsymbol{q}|)\right]}{\hbar(\omega+i0^+)+\varepsilon_\gamma^\nu(k)-\varepsilon_{\gamma'}^\nu(|\boldsymbol{k}+\boldsymbol{q}|)},\end{aligned} \tag{6}$$

where $\Theta_0(x)$ stands for a unit-step function, and $\gamma = \pm1$ stands for the electron or hole state with energy dispersions above or below the Dirac point. Moreover, the index ν, which equals to $\sigma\xi = \pm1$ for buckled honeycomb lattices or molybdenum disulfide, specifies two different pairs of degenerate subbands from Eq. (1) or Eq. (3).

Finally, the full polarization function at zero temperature is obtained as

$$\Pi_0(q,\omega|E_F) = \sum_{\nu=\pm1}\Pi_0^{(\nu)}(q,\omega|E_F). \tag{7}$$

If the dispersions of low-energy subbands do not depend on the valley or spin indices ξ and σ, summation in Eq. (7) simply gives rise to a factor of two, as we have obtained for graphene.

Integral transformation in Eq. (5), which is used to obtain the finite-temperature polarization function from its zero-temperature counterparts with different Fermi energies, was first introduced in Ref. [34]. It could be derived in a straightforward way by noting that the only quantity which substantially depends on temperature in Eq. (6) is the Fermi-Dirac distribution function $n_F\left[\varepsilon_\gamma^\nu(k)-\mu(T)\right]$. It changes to the unit-step functions $\Theta_0\left[E_F-\varepsilon_\gamma^\nu(k)\right]$ at $T=0$, as used in Eq. (6). As the temperature T increases from zero, the distribution function in Eq. (6) evolves into [35, 36]

$$\begin{aligned}n_F\left[\varepsilon_\gamma^\nu(k)-\mu(T)\right] &= \frac{1}{2}\left[1-\,\tanh\left(\frac{\varepsilon_\gamma^\nu(k)-\mu(T)}{2k_BT}\right)\right]\\ &= \int_0^\infty d\eta\,\frac{\Theta_0\left[\mu(T)-\varepsilon_\gamma^\nu(k)\right]}{4k_BT\cosh^2\{[\mu(T)-\eta]/2k_BT\}}.\end{aligned} \tag{8}$$

For accessible temperatures, the energy dispersions $\varepsilon_\gamma^\nu(k)$, corresponding wave functions and their overlap factors are all temperature independent. As a result, the polarization function is expected to be modified by the same integral transformation, or a convolution, as each of the Fermi-Dirac distribution function in the numerator of Eq. (6).

We first look at intrinsic plasmons with $E_F = 0$ at $T = 0$. In this case, $\mu(T)$ also remains at the Dirac point for any temperature T. As T increases to $k_BT \gg E_F > 0$, on the other hand, $\Pi_0(q, \omega|E_F)$ for gapless graphene gives rise to a plasmon dispersion $\omega_p \simeq q\,T$ in the long-wave limit and the damping rate is $\sim q^{3/2}/\sqrt{T}$. As a result, the plasmon mode becomes well defined [6] for $q < 16\epsilon_0\epsilon_r k_B T/\pi e^2$.

Additionally, finite-T polarization function $\Pi_T\left(q, \omega|\mu_T, \Delta_\beta\right)$ of a 2D material is directly related to its optical conductivity $\sigma_O^{(T)}\left(\omega|\mu_T, \Delta_\beta\right)$ through [19]

$$\sigma_O^{(T)}\left(\omega|\mu_T, \Delta_\beta\right) = i\omega e^2 \lim_{q\to 0} \frac{\Pi_T\left(q, \omega|\mu_T, \Delta_\beta\right)}{q^2}, \tag{9}$$

where we introduce the notation $\mu_T \equiv \mu(T)$, $\Pi_T\left(q, \omega\,|\mu_T, \Delta_\beta\right) \sim q^2$ as $q \to 0$ for each of our considered 2D materials, regardless of their band structure, as given by Eq. (47) for $T = 0$. This conclusion holds true even for finite T and makes the optical conductivity independent of q, and therefore the $q \to 0$ limit in Eq. (9) becomes finite.

From Eq. (9), we find explicitly that

$$\begin{aligned}
\mathrm{Im}\left[\sigma_O^{(0)}\left(\omega|E_F, \Delta_\beta\right)\right] &= \frac{e^2}{4\pi\hbar}\sum_{\beta=\pm 1}\left\{\frac{4E_F}{\hbar\omega}\left[1-\left(\frac{\Delta_\beta}{E_F}\right)^2\right] + \left[1+\left(\frac{2\Delta_\beta}{\hbar\omega}\right)^2\right]\ln\left|\frac{2E_F-\hbar\omega}{2E_F+\hbar\omega}\right|\right\},\\
\mathrm{Re}\left[\sigma_O^{(0)}\left(\omega|E_F, \Delta_\beta\right)\right] &= \frac{e^2}{4\hbar}\,\Theta(\hbar\omega - 2E_F)\sum_{\beta=\pm 1}\left[1+\left(\frac{2\Delta_\beta}{\hbar\omega}\right)^2\right].
\end{aligned} \tag{10}$$

Here, the *state-blocking effect* due to Pauli exclusion principle directly results in the diminishing of the real part of the optical conductivity at zero temperature for $\hbar\omega < 2E_F$. However, if $T > 0$, such state-blocking effect will not exist [37–40] due to

$$\Theta\left(E_F - \varepsilon_\beta^\gamma(k)\right) \Rightarrow \frac{1}{2}\left\{1 - \tanh\left[\frac{\varepsilon_\beta^\gamma(k) - \mu_T}{2k_BT}\right]\right\}. \tag{11}$$

Furthermore, for gapless ($\Delta_\beta = 0$) but doped ($E_F > 0$) graphene in the high-T limit we obtain from Eq. (10)

$$\begin{aligned}
\sigma_O^{(T)}\left(\omega|\mu_T, \Delta_\beta = 0\right) \simeq \frac{e^2}{\hbar}\Bigg\{&\frac{\hbar\omega}{16k_BT}\left[1-\frac{1}{3}\left(\frac{\hbar\omega}{4k_BT}\right)^2\right]\\
&+ i\,\frac{2\ln 2k_BT}{\pi\hbar\omega}\left[1+2\ln 2\left(\frac{E_F}{4\ln 2k_BT}\right)^4\right]\Bigg\},
\end{aligned} \tag{12}$$

where we have used the high-T limit [17] for the chemical potential $\mu_T \approx \left(E_F^2/4\ln 2k_BT\right)$. In either case above, we have to present analytical expression for $\mu(T)$ as a function of T so as to gain the explicit T dependence of optical conductivity. From Eq. (12) we conclude that $\mathrm{Im}\left[\sigma_O^{(T)}\left(\omega|\mu_T, \Delta_\beta = 0\right)\right]$ depends weakly on E_F.

On the other hand, for gapped ($\Delta_\beta = \Delta_0$) but undoped ($E_F = 0$) graphene at high T ($k_BT \gg \Delta_0$ and $\hbar\omega$), we get its optical conductivity [41]

$$\mathrm{Re}\left[\sigma_O^{(T)}(\omega|\mu_T, \Delta_0)\right]_{E_F=0} = \frac{e^2}{16\hbar}\left(\frac{\hbar\omega}{k_BT}\right)\left(1 - \frac{\Delta_0}{\hbar\omega}\right),$$

$$\mathrm{Im}\left[\sigma_O^{(T)}(\omega|\mu_T, \Delta_0)\right]_{E_F=0} = \frac{4e^2}{\pi\hbar}\left(\frac{k_BT}{\hbar\omega}\right)\left\{2\ln 2 - \left(\frac{\Delta_0}{k_BT}\right)^2\left[\mathbb{C}_0 - \ln\left(\frac{\Delta_0}{2k_BT}\right)\right]\right\}, \tag{13}$$

where the constant $\mathbb{C}_0 \simeq 0.79$ appears due to a finite bandgap. [36].

4. Chemical potential at finite temperatures

As we have seen from Section 3, we need know $\mu(T)$ as a function of T explicitly so as to gain T dependence of polarization function, plasmon, transport and optical conductivities, or any other quantities related to collective behaviors of 2D materials at finite temperatures [42].

The density of states (DOS), which plays an important tool in calculating electron (or hole) Fermi energy E_F and chemical potential $\mu(T)$, is defined as

$$\rho_d(\mathbb{E}) = \sum_{\gamma=\pm1}\sum_{\xi,\,\sigma=\pm1}\int \frac{d^2\boldsymbol{k}}{(2\pi)^2}\,\delta\Big(\mathbb{E} - \varepsilon^{\gamma}_{\xi,\sigma}(k)\Big), \tag{14}$$

where $\delta(x)$ is Dirac delta function. Using Eq. (14), we immediately obtain a piece-wise linear function for silicene [43]

$$\rho_d(\mathbb{E}) = \frac{1}{\pi}\sum_{\gamma=\pm1}\frac{\gamma\,\mathbb{E}}{\hbar^2 v_F^2}\sum_{i=<,>}\Theta_0\left(\frac{\mathbb{E}}{\gamma} - \Delta_i\right). \tag{15}$$

This result is equivalent to the DOS of graphene except that there are no states within the bandgap region, as demonstrated by two unit-step functions $\Theta_0(|\mathbb{E}|-\Delta_<)$ and $\Theta_0(|\mathbb{E}|-\Delta_>)$.

Finally, the chemical potential $\mu(T)$ can be calculated using the *conservation of the difference of electron and hole densities*, [17] $n_e(T)$ and $n_h(T)$, for all temperatures including $T = 0$, i.e.,

$$n = n_e(T) - n_h(T) = \int_0^\infty d\mathbb{E}\rho_d(\mathbb{E})f_{\gamma=1}(\mathbb{E}, T) - \int_{-\infty}^0 d\mathbb{E}\rho_d(\mathbb{E})\Big[1 - f_{\gamma=1}(\mathbb{E}, \mathbb{T})\Big], \tag{16}$$

where $f_{\gamma=1}(\mathbb{E}, T) = \{1 + \exp[(\mathbb{E} - \mu(T))/k_BT]\}^{-1}$ is the Fermi function for electrons in thermal equilibrium. The hole distribution function is just $f_{\gamma=-1}(\mathbb{E} < 0, T) = 1 - f_{\gamma=1}(\mathbb{E}, T)$.

At $T = 0$, it is straightforward to get the Fermi energy E_F from Eq. (16) for silicene

$$E_F^2 - \frac{1}{2}\left(\Delta_>^2 + \Delta_<^2\right) = (\hbar v_F)^2\pi n. \tag{17}$$

where we have assumed that both subbands are occupied for simplicity. The discussions of other cases can be found from Ref. [18]. Consequently, minimum electron density required to occupy the upper subband of silicene is $n_c = 2\Delta_{SO}\Delta_z/\pi\hbar^2 v_F^2$.

On the other hand, by applying Eq. (16), in combination with DOS in Eq. (15), for silicene, a transcendental (non-algebraic) equation [43, 44] could be obtained for $\mu(T)$, that is

$$\left(\frac{\hbar v_F}{k_B T}\right)^2 n = \frac{1}{\pi}\sum_{\gamma=\pm 1}\gamma \sum_{i=<,>}\left\{-\mathrm{Li}_2\left(-\exp\left[\frac{\gamma\mu(T)-\Delta_i}{k_B T}\right]\right) + \frac{\Delta_i}{k_B T}\ln\left(1+\exp\left[\frac{\gamma\mu(T)-\Delta_i}{k_B T}\right]\right)\right\}, \tag{18}$$

where $\mathrm{Li}_2(x)$ is a polylogarithm or dilogarithm function, defined mathematically by

$$\mathrm{Li}_2(z) = -\int_0^z dt\left[\frac{\ln(1-t)}{t}\right]. \tag{19}$$

Interestingly, the right-hand side of Eq. (18) contains terms corresponding to both pristine and gapless graphene, using which we find from Ref. [17].

$$\frac{1}{2(k_B T)^2}E_F^2 = -\sum_{\gamma=\pm 1}\gamma\,\mathrm{Li}_2\left\{-\exp\left[\frac{\gamma\mu(T)}{k_B T}\right]\right\}, \tag{20}$$

as well as a well-known analytical expression for $\mu_0(T)$ of 2D electron gas with Schrödinger-based electron dynamics

$$\mu_0(T) = k_B T\,\log\left(1+\exp\left[\frac{\pi\hbar^2 n_0}{m^* k_B T}\right]\right). \tag{21}$$

An advantage of Eq. (18) is that it could be solved even without taking an actual integration. In fact, one can either readily solve it numerically using some standard computational algorithms, or introduce an analytical approximation to the sought solution near specific temperature assigned.

Numerical results for $\mu(T)$ of silicene are presented in **Figure 3**. In all cases, $\mu(T)$ decreases with increasing T from zero. However, it is very important to notice that

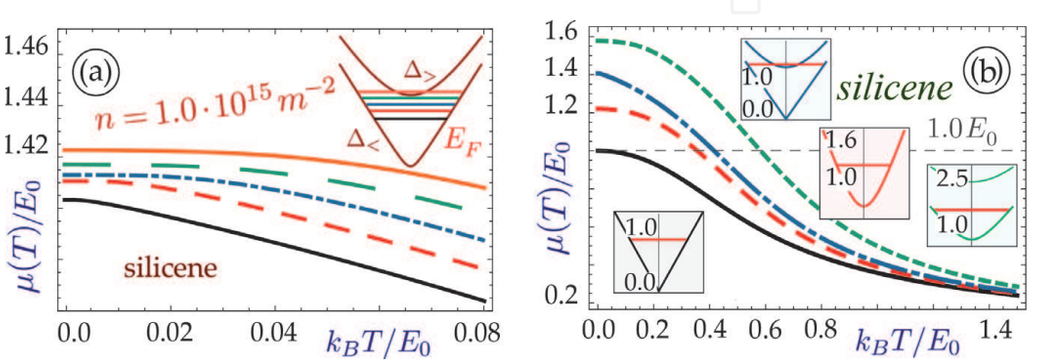


Figure 3.
Temperature dependence of the chemical potential μ(T) *for silicene with two inequivalent energy subbands with various bandgaps and a fixed doping density* $\mathrm{n} = 1 \times 10^{11}\,cm^{-2}$. *Panel (a) highlights the situation close to* $\mathrm{T} = 0$, *while panel (b) shows the whole temperature range. Here,* E_0 *is the Fermi energy of graphene.*

$\mu(T)$ never reaches zero or changes its sign in the systems with an electron–hole symmetry due to increasing contribution from holes in Eq. (16). All of displayed results in **Figure 3** depend on individual bandgaps $\Delta_<$ and $\Delta_>$. The special case with $\Delta_< = \Delta_>$ corresponds to gapped graphene, for which plasmon modes at $T = 0$ were studied in Ref. [33]. The graphene Fermi wave number is $k_F = \sqrt{\pi n}$, irrelevant to its bandgap. The general relation between k_F and n in 2D materials is given by $(2\pi)^2 n = g\pi k_F^2$. The experimentally allowable electron (or hole) doping is within the range of $n = 10^{10} - 10^{12}$ cm^{-2}, leading to $k_F = 10^6 - 10^7$ cm^{-1}. For two pair of inequivalent subbands, such as in silicene or MoS_2, there are two different Fermi wave numbers for these subbands. Moreover, the numerically calculated $\mu(T)$ as functions of T for electron and hole doping are presented in **Figure 4**. In this case, however, there exists no electron-hole symmetry, and therefore the resulting $\mu(T)$ can be zero and change its sign as T increases, in contrast to the results in **Figure 3**.

Eq. (18) could also be applied to a wide range of 2D materials if its DOS has a linear dependence on energy $\mathbb{E}$. Particularly, it is valid for calculating the finite-T chemical potential of TMDC's with an energy dispersion presented in Eq. (3). However, we are aware that some terms in Eq. (3) for TMDC's, which might be insignificant for dispersions of other 2D materials, become essential in DOS because of very large bandgap and mass terms around $k = 0$. As an estimation, for $k/k_0 \approx 5.0$, the correction term $\simeq \beta\Delta k^4$ must be taken into account. Meanwhile, the highest accessible doping $n = 10^{13}$ cm^{-2} only gives rise to a Fermi energy $E_F \sim \lambda_0$, comparable to spin-orbit coupling.

Now, we turn to calculate $\mu(T)$ as a function of T for MoS_2 with a much more complicated band structure. After taking into account the $\sim k^2$ mass terms, we are able to write down [18]

$$\rho_d(\mathbb{E}) = \frac{1}{2\pi\hbar^2}\sum_{\gamma,\nu=\pm1}\left|\frac{\alpha+\gamma\beta}{4m_e} + \frac{\gamma(t_0a_0)^2}{\hbar^2(\Delta-\nu\lambda_0)}\right|^{-1}\Theta_0\left(\gamma\left[\mathbb{E}-\frac{\nu\lambda_0}{2}\right]-\frac{1}{2}(\Delta-\nu\lambda_0)\right), \tag{22}$$

where the calculation is based on a parabolic-subband approximation, i.e.,

$$\varepsilon_\gamma^\nu(k) = \frac{1}{2}[\nu\lambda_0(1-\gamma)+\gamma\Delta] + \left[\frac{\hbar^2}{4m_e}(\alpha+\gamma\beta) + \frac{\gamma(t_0a_0)^2}{\Delta-\nu\lambda_0}\right]k^2. \tag{23}$$

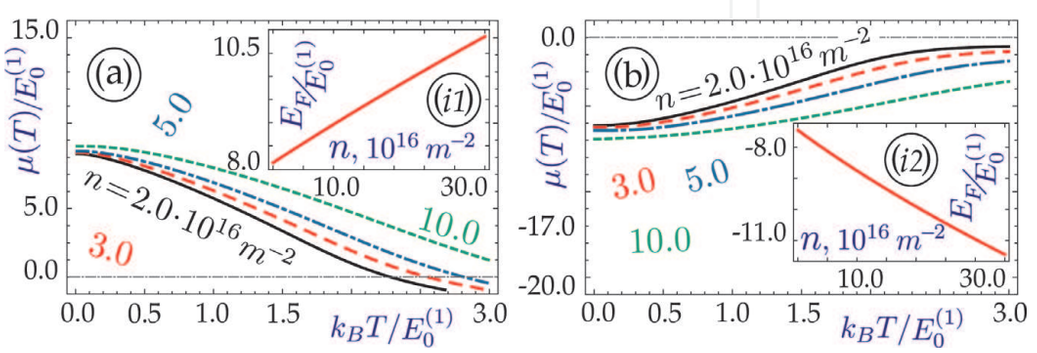


Figure 4.
Temperature dependence of the chemical potential μ(T) for molybdenum disulfide for cases of electron (a) and hole (b) doping with various doping densities. μ(T) might change its sign in contrast to the previously considered graphene and silicene. The two insets demonstrate how the Fermi energy depends on the electron and hole doping densities, correspondingly.

From Eq. (22), we further seek an explicit expression for DOS in the form a piecewise-linear function of energy $\mathbb{E}$: $\rho_d(\mathbb{E}) = A_i + B_i\mathbb{E}$. A complete set of expressions for DOS of MoS_2 has been reported in Ref. [18]. Here, we merely provide and discuss these DOS expression around the lower hole subband with $\mathbb{E} \approx -\Delta/2 - \lambda_0$, yielding

$$\rho_d(\mathbb{E}) = c_0^{(1)} + \left[\mathbb{E} - \left(\frac{\Delta}{2} + \lambda_0\right)\right] c_1^{(1)},$$

$$c_0^{(1)} = \frac{1}{2\pi} \sum_{\nu=\pm 1} \frac{\Delta - \nu\lambda_0}{(a_0 t_0)^2 + (\beta - \alpha)(\Delta - \nu\lambda_0)},$$

$$c_1^{(1)} = \frac{1}{\pi} \sum_{\nu=\pm 1} \frac{\left[(a_0 t_0)^2 + \hbar^2\beta/(4m_e)(\Delta - \nu\lambda_0)\right]^2 \delta\varepsilon}{\left\{(a_0 t_0)^2 + \hbar^2/(4m_e)[(\beta - \alpha)(\Delta - \nu\lambda_0)]\right\}^3} < 0, \tag{24}$$

or numerically,

$$c_0^{(1)} = 0.233 \frac{1}{t_0 a_0^2} = 15.17 \frac{E_0}{(\hbar v_F)^2},$$

$$c_1^{(1)} = -0.458 \frac{1}{(t_0 a_0)^2} = -2.077 \frac{1}{(\hbar v_F)^2}. \tag{25}$$

The calculated numerical results for DOS in all regions are listed in **Table 1**. All introduced coefficients $c_0^{(i)}, c_1^{(i)}$ for $i = 1, 2, 3$ can be deduced from the calculated parameters A_i and B_i using a similar correspondence as in Eq. (24).

The critical doping density which is required to populate the lower hole subband in MoS_2 is found to be

$$n_c = \frac{2}{\pi} \frac{\lambda_0 \Delta}{(t_0 a_0)^2} = 1.0 \times 10^{14}\ \text{cm}^{-2}. \tag{26}$$

Therefore, for most experimentally accessible densities $n \leq 10^{13}\ \text{cm}^{-2}$, the lower hole subband still could not be populated at $T = 0$.

Next, we would evaluate both sides of Eq. (16) for MoS_2. As an example, we consider electron doping with density $n_e > 0$. The electron Fermi energy E_F^e is determined by the following relation

$$n_e = \frac{c_1^{(3)}}{2}\left[\left(E_F^e\right)^2 - \frac{\Delta^2}{4}\right] + c_0^{(3)}\left(E_F^e - \frac{\Delta}{2}\right). \tag{27}$$

From Eq. (27), we can easily find the electron Fermi energy $E_F > 0$ as

Range index	Energy range	γ	ν	$A_i[1/(t_0 a_0^2)]$	$B_i[1/(t_0 a_0)^2]$
$i = 1$	$\mathbb{E} < -\Delta/2 - \lambda_0$	-1	$+1$	0.0174	-0.169
$i = 2$	$\lvert\mathbb{E} + \Delta/2\rvert < \lambda_0$	-1	-1	0.043	-0.308
$i = 3$	$\mathbb{E} > \Delta/2$	$+1$		0.078	$+0.179$

Table 1.
Linearized density of states (DOS) $\rho_d(\mathbb{E}) = A_i + B_i\mathbb{E}$ of MoS_2 for all three energy regions. Here, the DOS within the gap region, $-\Delta/2 + \lambda_0 < \mathbb{E} < \Delta/2$, is zero.

$$E_F^e = \frac{1}{c_1^{(3)}}\left[-c_0^{(3)} + \sqrt{\left(c_0^{(3)} + c_1^{(3)}\,\frac{\Delta}{2}\right)^2 + 2n_e c_1^{(3)}}\right]. \tag{28}$$

In a similar way, for hole doping with density n_h and the Fermi energy E_F^h located between two hole subbands (region 2), we find

$$|E_F^h| = \frac{1}{c_1^{(2)}}\left\{\sqrt{\left[c_0^{(2)} - c_1^{(2)}\left(\frac{\Delta}{2} - \lambda_0\right)\right]^2 - 2n_h c_1^{(2)}} - c_0^{(2)}\right\}, \tag{29}$$

where $c_1^{(2)} < 0$ and $\mathbb{E} < -\Delta/2 + \lambda_0$. From Eq. (29) we easily find the doping density

$$n_h = \left(\frac{\Delta}{2} + E_F^h - \lambda_0\right)\left[c_0^{(2)} + \frac{c_1^{(2)}}{2}\left(\frac{\Delta}{2} - \left(E_F^h + \lambda_0\right)\right)\right]. \tag{30}$$

The right-hand side of Eq. (16) for TMDC's could be expressed as a combination of electron and hole contributions $\mathcal{I}_e(\Delta|T) - \mathcal{I}_h(\Delta, \lambda_0|T)$. Here, we will introduce two self-defined functions

$$\begin{aligned}
\mathcal{A}_0(\mathbb{E}, T) &= \left[1 + \exp\left(\frac{\mathbb{E} - \mu(T)}{k_B T}\right)\right]^{-1}, \\
\mathcal{A}_1(\mathbb{E}, T) &= \mathbb{E}\,\mathcal{A}_0(\mathbb{E}, T) = \mathbb{E}\left[1 + \exp\left(\frac{\mathbb{E} - \mu(T)}{k_B T}\right)\right]^{-1},
\end{aligned} \tag{31}$$

so that

$$\mathcal{I}_e(\Delta|T) = \sum_{j=0}^{1} c_j^{(3)} \int_{\Delta/2}^{\infty} d\mathbb{E}\,\mathcal{A}_j(\mathbb{E}, T). \tag{32}$$

For convenience, we introduce another function $\mathcal{R}_p(T, X)$

$$\mathcal{R}_p(T, X) = \int_0^{\infty} d\xi\,\frac{\xi^p}{1 + \exp\left(\xi - X/k_B T\right)}, \tag{33}$$

where $\xi = (\mathbb{E} - \Delta_<)/k_B T$. Consequently, we are able to rewrite Eq. (32) as

$$\mathcal{I}_e(\Delta\,|\,T) = k_B T\left(c_0^{(3)} + \frac{\Delta}{2}\right)\mathcal{R}_0\left(T, \mu(T) - \frac{\Delta}{2}\right) + c_1^{(3)}(k_B T)^2\,\mathcal{R}_1\left(T, \mu(T) - \frac{\Delta}{2}\right), \tag{34}$$

where two terms with $p = 0, 1$ are physically related to a 2D electron gas. Explicitly, Eq. (33) leads to

$$\begin{aligned}
\mathcal{R}_0(T, X) &= \ln\left(1 + \exp\left(\frac{X}{k_B T}\right)\right), \\
\mathcal{R}_1(T, X) &= -\mathrm{Li}_2\left(-\exp\left(\frac{X}{k_B T}\right)\right),
\end{aligned} \tag{35}$$

Using these self-defined functions and their notations, we finally arrive at the "*hole term*" $\mathcal{I}_h(\Delta,\lambda_0|T)$ in Eq. (16)

$$\begin{aligned}\int_{-\infty}^{0} d\mathbb{E}\rho_d(|\mathbb{E}|)\left[1-f_1(\mathbb{E},\mathbb{T})\right] &= \int_{-\infty}^{-\Delta/2+\lambda_0} d\mathbb{E}\left(c_0^{(2)}-c_1^{(2)}\mathbb{E}\right)\left[1+\exp\left(\frac{\mu(T)-\mathbb{E}}{k_BT}\right)\right]^{-1} \\ &+ \int_{-\infty}^{-\Delta/2-\lambda_0} d\mathbb{E}\left(\delta c_0^{(1)}-\delta c_1^{(1)}\mathbb{E}\right)\left[1+\exp\left(\frac{\mu(T)-\mathbb{E}}{k_BT}\right)\right]^{-1} \\ &\equiv \sum_{j=1}^{4}\mathcal{I}_h^{(j)}(\Delta,\lambda_0|T),\end{aligned} \tag{36}$$

where $\delta c_i^{(1)} = c_i^{(1)} - c_i^{(2)}$ for $i = 0, 1$, and

$$\begin{aligned}\mathcal{I}_h^{(1)}(\Delta,\lambda_0|T) &= k_BT\left(\frac{\Delta}{2}-\lambda_0+c_2^{(0)}\right)\mathcal{R}_0(T,-[\mu(T)+\Delta/2-\lambda_0]),\\ \mathcal{I}_h^{(2)}(\Delta,\lambda_0|T) &= c_2^{(1)}(k_BT)^2\mathcal{R}_1(T,-[\mu(T)+\Delta/2-\lambda_0]),\\ \mathcal{I}_h^{(3)}(\Delta,\lambda_0|T) &= k_BT\left(\frac{\Delta}{2}+\lambda_0+\delta c_1^{(0)}\right)\mathcal{R}_0(T,-[\mu(T)+\Delta/2+\lambda_0]),\\ \mathcal{I}_h^{(4)}(\Delta,\lambda_0|T) &= \delta c_1^{(1)}(k_BT)^2\mathcal{R}_1(T,-[\mu(T)+\Delta/2+\lambda_0]).\end{aligned} \tag{37}$$

Here, both $\mathcal{I}_e(\Delta|T)$ in Eq. (34) and $\mathcal{I}_h(\Delta,\lambda_0|T)$ in Eq. (36) comprise a finite-temperature part for the right-hand side of Eq. (16). Its left-hand side has already been given by Eq. (27). From these results, it is clear that there exists no symmetry between the electron and hole states at either zero or finite T. Finally, $\mu(T)$ of TMDC's could be computed from a transcendental equation in Eq. (18), similarly to finding $\mu(T)$ for silicene.

By using the calculated $\mu(T)$, the plasmon dispersions and their Landau damping, determined from Eqs. (4) and (5), are displayed in **Figure 5** for silicene at different T. Comparison of panels (a) and (b) indicates that the T dependence of plasmon damping is not uniform even on a fixed convolution path $\mu(T)$. The doping

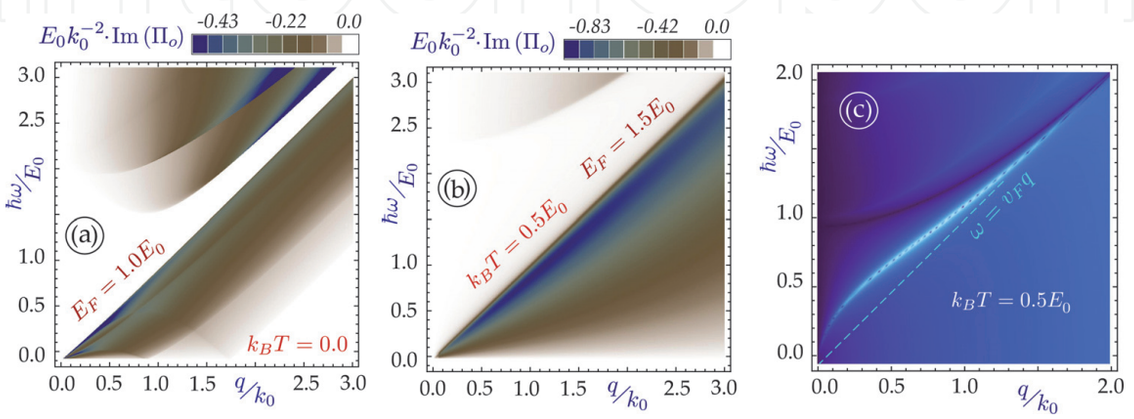


Figure 5.
Particle-hole modes and plasmon branch for extrinsic (doped) silicene layer at a finite temperature. Panels (a) and (b) show two comparative graphs for $\mathrm{Im}[\Pi_0(\mathrm{q},\omega|\mu(\mathrm{T}))]$ *at zero and finite* T*, respectively, while plot (c) presents the finite-*T *plasmon branch with* $\mu(\mathrm{T})$ *calculated from Eq. (16).*

density, on the other hand, widens the plasmon damping-free regions. Therefore, both the thermal and doping effects are found to compete with each other in dominating the plasmon dampings through selecting different convolution paths $\mu(T)$ with various doping densities or Fermi energies. Furthermore, the plasmon energy in (c) is pushed up slightly by increasing doping density at finite T.

5. Dice lattice and α-$\mathcal{T}_3$ materials

In addition to graphene and silicene, another type of Dirac-cone materials is the one with fermionic states in which multiple Dirac points evolve into a middle flat band. One of the first fabricated materials with such a flat band is a dice or a $\mathcal{T}_3$ lattice, for which its atomic composition consists of hexagons similarly to graphene, but with an additional atom at the center of each hexagon. In a dice lattice, the bond coupling between a central site and three nearest neighbors is the same as that between atoms on corners, while for an α-$\mathcal{T}_3$ model the ratio α between hub-rim and rim-rim hopping coefficients can vary [45, 46] within the range of $0 < \alpha < 1$.

The low-energy electronic states of α-$\mathcal{T}_3$ materials are specified by a 3×3 pseudospin-1 Dirac Hamiltonian, which results in three solutions for the energy dispersions and includes one completely flat and dispersionless band with $\varepsilon_0(k) \equiv 0$. The other two bands are equivalent to Dirac cone $\varepsilon_\pm(k) = \pm\hbar v_F k$ in graphene with the same Fermi velocity $v_F = 10^8$ cm/s. All of three bands touch at the corners of the first Brillouin zone, and therefore the band structure becomes metallic. In addition, the flat band has been shown to be stable against external perturbations, magnetic fields and structure disorders [47].

The α-$\mathcal{T}_3$ model was initially considered only as a theoretical contraption, an interpolation between graphene and a dice lattice. As parameter $\alpha \to 0$, this structure approaches graphene and a completely decoupled system of the hub atoms at the centers of each hexagon. A bit later, first evidence of really existing or fabricated materials with α-$\mathcal{T}_3$ electronic structure began mounting up. This includes Josephson arrays, optical arrangement based on the laser beams, Kagome and Lieb lattices with optical waveguides, $Hg_{1-x}Cd_xTe$ for a specific electron doping density, dielectric photonic crystals having zero-refractive index and a few others [48, 49]. So far, α-$\mathcal{T}_3$ model is believed to be the most promising innovative low-dimensional systems, and is one of the mostly investigated material in modern condensed matter physics. The most important technological application of α-$\mathcal{T}_3$ rests on the availability of materials with various α values, i.e., with small and large rim-hub hopping coefficients, ranging from $\alpha = 0$ for graphene up to $\alpha = 1$ for a dice lattice.

The low-energy Dirac-Weyl Hamiltonian for the α-$\mathcal{T}_3$ model is [45]

$$\hat{\mathbb{H}}_\xi^\phi(\boldsymbol{k}) = \hbar v_F \begin{bmatrix} 0 & k_-^\xi \cos\phi & 0 \\ k_+^\xi \cos\phi & 0 & k_-^\xi \sin\phi \\ 0 & k_+^\xi \sin\phi & 0 \end{bmatrix}, \tag{38}$$

where $\boldsymbol{k} = (k_x, k_y)$ is the electron wave vector, $k_\pm^\xi = \xi k_x \pm i k_y$, $\xi = \pm 1$ corresponds to two different valleys, and v_F is the Fermi velocity. Here, the parameter α is related to the geometry phase $\phi = \tan^{-1}\alpha$ which directly enters into the Hamiltonian in Eq. (38). The phase ϕ possesses a fixed, one-to-one correspondence to the Berry phase of electrons in α-$\mathcal{T}_3$ model. In particular, for $\alpha = 1$ or $\phi = \pi/4$ we get a dice lattice with its Hamiltonian given by [50].

$$\hat{\mathbb{H}}_{\xi}^{d}(\boldsymbol{k}) = \frac{\hbar v_F}{\sqrt{2}} \begin{bmatrix} 0 & k_{-}^{\xi} & 0 \\ k_{+}^{\xi} & 0 & k_{-}^{\xi} \\ 0 & k_{+}^{\xi} & 0 \end{bmatrix}. \tag{39}$$

Three energy bands from Hamiltonian in Eq. (38) or Eq. (39) are $\varepsilon_0^{\gamma}(k) = \gamma\hbar v_F k$ for valence ($\gamma = -1$), conduction ($\gamma = +1$) and flat ($\gamma = 0$) bands. These energy bands are degenerate with respect to ξ and phase ϕ. The corresponding wave functions for the valence and conduction bands take the form

$$\Psi_0^{\gamma=\pm1}(\boldsymbol{k}|\xi,\phi) = \frac{1}{\sqrt{2}} \begin{bmatrix} \xi\cos\phi\, e^{-i\xi\theta_{\mathbf{k}}} \\ \gamma \\ \xi\sin\phi\, e^{i\xi\theta_{\mathbf{k}}} \end{bmatrix}, \tag{40}$$

where $\tan\theta_{\mathbf{k}} = k_y/k_x$. Meanwhile, for the flat band, we find

$$\Psi_0^{\gamma=0}(\boldsymbol{k}\,|\xi,\phi) = \begin{bmatrix} \xi\sin\phi\, e^{-i\xi\theta_{\mathbf{k}}} \\ 0 \\ -\xi\cos\phi\, e^{i\xi\theta_{\mathbf{k}}} \end{bmatrix}. \tag{41}$$

Here, the components of wave functions in Eqs. (40) and (41) depend on valley index ξ and phase ϕ, which leads to the same dependence on all collective properties of an α-$\mathcal{T}_3$ materials, including plasmon dispersion.

Now we turn to deriving plasmon branches and their damping rates at finite T in α-$\mathcal{T}_3$ model. The computation procedure is quite similar to that in the case of two non-equivalent doubly degenerate subband pairs, including silicene, germanene and MoS_2 discussed in Section 4.

For α-$\mathcal{T}_3$ model, the finite-T polarization function $\Pi_T(q,\omega|\mu(T))$ can be obtained by an integral transformation of its zero-temperature counterpart $\Pi_0(q,\omega|E_F)$, as presented in Eq. (5). In this case, the zero-T counterpart $\Pi_0(q,\omega|E_F)$ is calculated as

$$\Pi_0(q,\omega|E_F) = \frac{1}{\pi^2}\sum_{\gamma,\gamma'=0,\pm1}\int d^2\boldsymbol{k}\mathbb{O}_{\gamma,\gamma'}(\boldsymbol{k},\boldsymbol{k}+\boldsymbol{q}|\phi) \times \frac{\Theta_0\left(E_F-\varepsilon_\gamma(k)\right)-\Theta_0\left(E_F-\varepsilon_{\gamma'}\left(|\boldsymbol{k}+\boldsymbol{q}|\right)\right)}{\hbar(\omega+i0^+)+\varepsilon_\gamma(k)-\varepsilon_{\gamma'}\left(|\boldsymbol{k}+\boldsymbol{q}|\right)}. \tag{42}$$

Structurally, Eq. (42) looks quite similarly to Eq. (6) for buckled honeycomb lattices and TMDC's. The most significant difference comes as the existence of an additional flat band with $\gamma = 0$ so that the summation index runs over ±1 and 0 instead of two. On the other hand, the overall expression for $\Pi_0(q,\omega|E_F)$ in Eq. (42) is simplified because the 4-fold degeneracy of each energy band independent of valley and spin index.

Here, we would limit our consideration to the case of electron doping with $n > 0$ and apply the random-phase approximation theory only for that case. For electron doping with $n > 0$, we can neglect the transitions within the valence band and also the transitions between the flat and valences bands due to full occupations of these electronic states. On the other hand, the overlap of initial and final electron transition states is defined by [51] $\mathbb{O}_{\gamma,\gamma'}^{\xi}(\boldsymbol{k},\boldsymbol{k}'|\phi,\lambda_0)$ with respect to the initial $\Psi_{\gamma}^{\xi}(\boldsymbol{k},\lambda_0)$ and the final $\Psi_{\gamma'}^{\xi}(\boldsymbol{k}',\lambda_0)$ states with a momentum transfer $\boldsymbol{q} = \boldsymbol{k}' - \boldsymbol{k}$, i.e.,

$$\mathbb{O}^{\xi}_{\gamma,\gamma'}(\boldsymbol{k},\boldsymbol{k}+\boldsymbol{q}|\phi,\lambda_0) = |\mathbb{S}^{\xi}_{\gamma,\gamma'}(\boldsymbol{k},\boldsymbol{k}+\boldsymbol{q}\,|\phi,\lambda_0|)^2,$$
$$\mathbb{S}^{\xi}_{\gamma,\gamma'}(\boldsymbol{k},\boldsymbol{k}+\boldsymbol{q}|\phi,\lambda_0) = \left\langle \Psi^{\xi}_{\gamma}(\boldsymbol{k},\lambda_0)\,|\Psi^{\xi}_{\gamma'}(\boldsymbol{k}+\boldsymbol{q},\lambda_0)\right\rangle, \tag{43}$$

where $\beta_{\mathbf{k},\mathbf{k}'} = \theta_{\mathbf{k}'} - \theta_{\mathbf{k}}$ is the scattering angle between two electronic states and $k' = \sqrt{k^2+q^2+2kq\,\cos\beta_{\mathbf{k},\mathbf{k}'}}$. Moreover, we find from Eq. (43) [52]

$$\mathbb{O}^{\xi}_{\gamma,\gamma'}(\boldsymbol{k},\boldsymbol{k}+\boldsymbol{q}|\phi,\lambda_0) = \frac{1}{4}\left[\left(1+\cos\beta_{\mathbf{k},\mathbf{k}'}\right)^2 + \cos^2(2\phi)\,\sin^2\beta_{\mathbf{k},\mathbf{k}'}\right] \tag{44}$$

for an arbitrary value of ϕ or α. It is easy to verify the known results $\left(1+\cos\beta_{\mathbf{k},\mathbf{k}'}\right)/2$ for graphene and $\left(1+\cos\beta_{\mathbf{k},\mathbf{k}'}\right)^2/4$ for a dice lattice as two limiting cases of our general result in Eq. (44) as $\alpha \to 0$ or $\alpha \to 1$, respectively. Furthermore, we find from Eq. (44) that the overlap does not depend on valley index ξ, even though individual wave function does, and then this index can be dropped. However, the valley-dependence in $\mathbb{O}^{\xi}_{\gamma,\gamma'}(\boldsymbol{k},\boldsymbol{k}+\boldsymbol{q}\,|\phi,\lambda_0)$ persists if α-$\mathcal{T}_3$ material is irradiated by circularly- or elliptically-polarized light. This incident radiation permits creating an valleytronic filter or any other types of valleytronic electron device.

Density plots for Landau damping with $\mathrm{Im}[\Pi_O(q,\omega|\mu(T))] \neq 0$ is presented in **Figure 6**, where we find plasmon branch will be completely free from damping within the region determined by $\hbar\omega/E_0 \leq 1$ and $q/k_0 \leq 1$, independent of geometry phase ϕ. On the other hand, another region with $\hbar\omega \leq \hbar v_F q$ (below the diagonal) becomes always Landau damped. Increasing T is able to increase greatly the damping in the region below the diagonal, as seen in **Figure 6(c)**.

In a correspondence to the damping of plasmons presented in **Figure 6**, we show in **Figure 7** the density plots for plasmon dispersions at $T = 0$ in (a), (b) and $k_BT = E_F$ in (c), (d). Comparing **Figure 7(a)** with **Figure 7(c)** we have clearly seen the thermal suppression of Landau damping for plasmon mode entering into a high-frequency region beyond $\hbar\omega = E_F$. To visualize a full plasmon dispersion clearly, we also include damped counterpart in **Figure 7(b)** and **(d)** at $T = 0$ and $k_BT = E_F$, respectively, where a significant enhancement of plasmon energy appears for large q values, moving upwards from the diagonal.

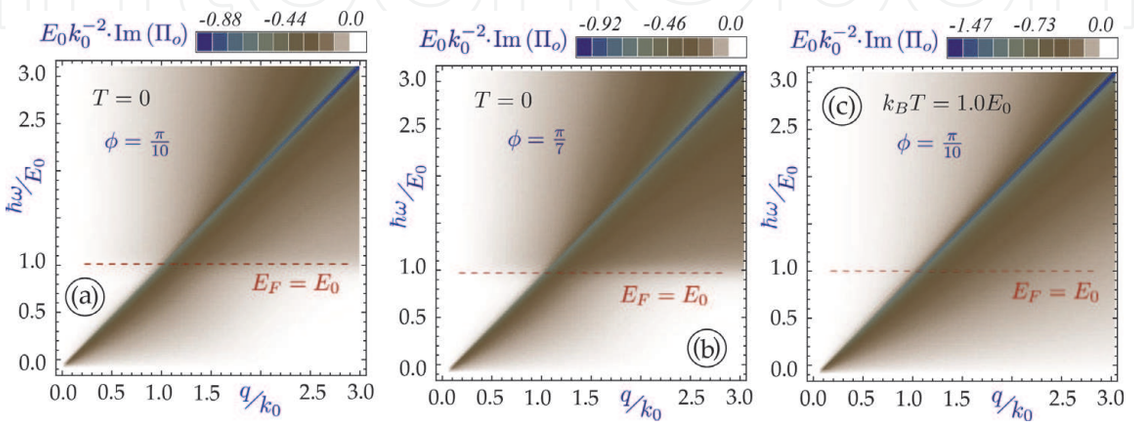


Figure 6.
Particle-hole modes, determined by non-zero $\mathrm{Im}[\Pi_O(q,\omega|\mu(T))]$ *within the* q-ω *plane, for an* α-$\mathcal{T}_3$ *layer with* $\phi = \pi/10$ *(in (a), (c)) and* $\phi = \pi/7$ *in (b). Panels (a) and (b) correspond to* $T = 0$, *while plot (c) is for* $k_BT = 1.0\,E_F$.

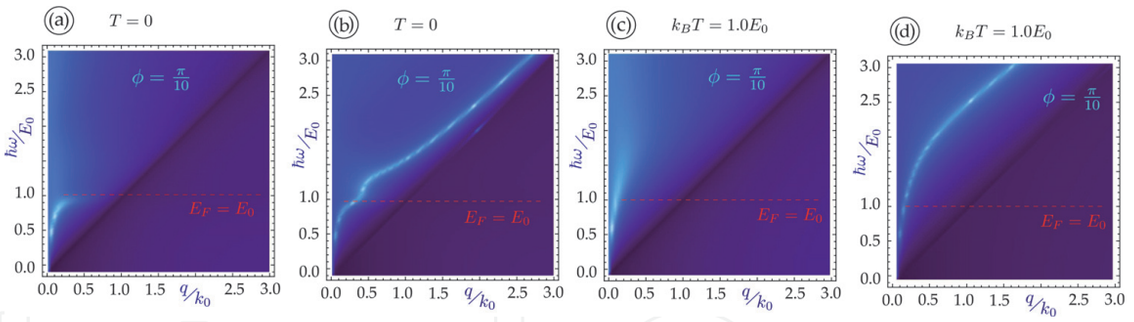


Figure 7.
Plasmon branches for an isolated α-$\mathcal{T}_3$ layer with $\phi = \pi/10$. Panels (a) and (c) only show undamped plasmons, while (b) and (d) display full plasmon branches including damped ones. Left panels (a) and (b) corresponds to $T = 0$, *while* $k_BT = 1.0E_F$ *for right panels (c) and (d).*

6. Plasmons in α-$\mathcal{T}_3$ layer coupled to conducting substrate

In the last part of THIS CHAPTER, WE WOULD LIKE TO FOCUS ON finite-T plasmons in a so-called nanoscale-hybrid structure consisting of a 2D layer, such as, graphene, silicene or a dice lattice, which is Coulomb-coupled to a large, conducting material. Physically, the Coulomb coupling between the 2D layer and the conductor results in a strong hybridization of graphene plasmon and localized surface-plasmon modes. This structure, which is referred to as an *open system*, could be realized experimentally or even by a device fabrication.

Our schematics for an open system is shown in **Figure 8**. The dynamical screening to the Coulomb interaction between electrons in a 2D layer and in metallic substrate is taken into account by a nonlocal and dynamical inverse dielectric function $\mathcal{K}(\boldsymbol{r}, \boldsymbol{r}'; \omega)$, as demonstrated in Refs. [53, 54]. This nonlocal inverse dielectric function is connected to a dielectric function $\epsilon(\boldsymbol{r}, \boldsymbol{r}'; \omega)$ in Eq. (4) by

$$\int d^3\boldsymbol{r}'\, \mathcal{K}(\boldsymbol{r}, \boldsymbol{r}'; \omega)\, \epsilon(\boldsymbol{r}', \boldsymbol{r}''; \omega) = \delta(\boldsymbol{r} - \boldsymbol{r}''), \tag{45}$$

and the resonances in $\mathcal{K}(\boldsymbol{r}, \boldsymbol{r}'; \omega)$ reveal the nonlocal hybridized plasmon modes supported by both 2D layer and the conducting surface as a single quantum system.

By using the Drude model for metallic substrate, the dielectric function can be written as $\epsilon_B(\omega) = 1 - \Omega_p^2/\omega^2$, where $\Omega_p = \sqrt{n_0 e^2/\epsilon_0 \epsilon_b m^*}$ is the bulk-plasma frequency for the conductor, n_0 electron concentration and m^* is the effective mass of electrons. Drude model describes electron screening in the long-wavelength limit. Based on the previously developed mean-field theory [53, 55, 56], we are able to

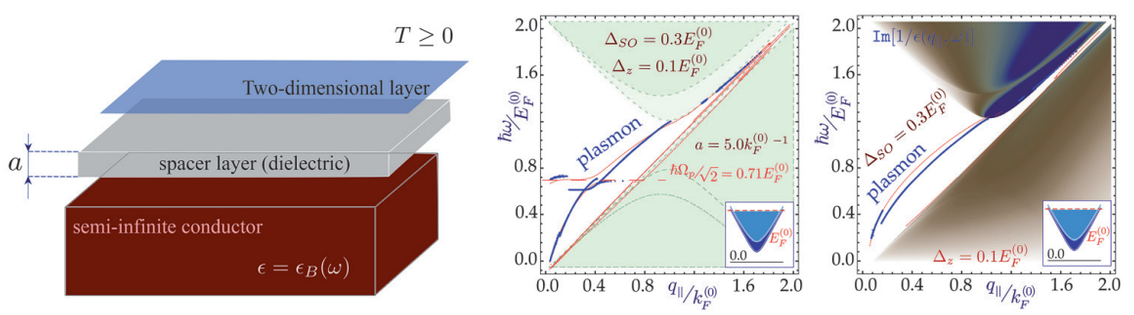


Figure 8.
Schematics for a silicene-based open system and numerical results for the two plasmon branches and their damping in this system with $\Delta_{SO} = 0.3E_0$ *and* $0.1E_0$, *where* $E_0 = \hbar v_F \sqrt{\pi n_0} = 54.6$ *meV.*

calculate plasmon dispersions in this 2D open system. For this, the plasmon dispersions are obtained from the zeros of the so-called *dispersion factor* $\mathbb{S}_C(q,\omega)$, instead of the dielectric function in Eq. (4). $\mathbb{S}_C(q,\omega)$ for this open system is given by [25, 54, 57]

$$\mathbb{S}_C(q,\omega|E_F) = 1 - \frac{2\pi\alpha_r}{q}\,\Pi_0(q,\omega|E_F)\left[1 + \frac{\Omega_p^2}{2\omega^2 - \Omega_p^2}\,\exp\left(-2qa\right)\right], \tag{46}$$

where a is the separation between the 2D layer and the conducting surface. Most important, we should emphasize that the second term in Eq. (46) does not have a full analogy with polarization function of an isolated layer, and the resulting plasmon dispersions in open system represents a hybridized plasmon mode with the environment. Therefore, these plasmon dispersions are expected to be sensitive to Coulomb coupling to electrons in the conducting substrate through a factor $\sim \exp\left(-2qa\right)$ in Eq. (46), similarly to what we have found for coupled double graphene layers [16]. The strong Coulomb coupling leads to a *linear dispersion* of plasmon in this open system [54, 58], which is in contrast with well-known $\sim \sqrt{q}$ dependence in all 2D materials.

As a special example, let us consider a silicene 2D layer with two bandgaps $\Delta_{<,>}$ and an electron doping density n. We start with seeking for a non-interacting polarization function in the long-wave limit $q \ll k_F^{<,>}$ for doping density n and assume a high-enough n to keep the Fermi level $E_F = \sqrt{\left(\hbar v_F k_F^{\beta}\right)^2 + \Delta_{\beta}^2} > \Delta_{>}$ above the large bandgap. Under this assumption, we get

$$\Pi_0(q,\omega|E_F) = \frac{q^2}{\pi\hbar^2\omega^2}\sum_{\beta=>,<} k_F^{\beta}\left|\frac{\partial\mathbb{E}_{\beta}(k)}{\partial k}\right|_{k=k_F^{\beta}} = \frac{E_F}{\pi}\left(2 - \frac{\Delta_<^2}{E_F^2} - \frac{\Delta_>^2}{E_F^2}\right)\frac{q^2}{\hbar^2\omega^2}, \tag{47}$$

where $k_F^{\beta} = \sqrt{2\pi n_{\beta}}$ are two different Fermi wave numbers associated with a single Fermi energy E_F, and n_{β} is the electron density for each subband satisfying $n = n_< + n_>$.

In the limit of $a \to \infty$, the plasmon branch of an isolated silicene layer can be recovered from Eq. (46), yielding

$$\omega_p^2(q) = \frac{4\alpha_r}{\hbar^2 E_F}\left(E_F^2 - \frac{\Delta_>^2 + \Delta_<^2}{2}\right)q \equiv \Xi q, \tag{48}$$

where for convenience we introduced a coefficient

$$\Xi\left(E_F,\Delta_{\beta}\right) = \frac{4\alpha_r}{\hbar^2 E_F}\left(E_F^2 - \frac{\Delta_>^2 + \Delta_<^2}{2}\right). \tag{49}$$

We notice from Eq. (48) that $\omega_p(q) \sim \sqrt{q}$, disregarding of the energy bandgaps $\Delta_{<,>}$ or doping density n. On the other hand, the Fermi energy E_F for silicene is given by Eq. (17).

Furthermore, using the notation defined by Eq. (49), we get from Eqs. (46) and (47) that

$$1 - \Xi\left(E_F,\Delta_{\beta}\right)\frac{q}{\omega^2}\left[1 + \frac{\Omega_p^2}{2\omega^2 - \Omega_p^2}\,\exp\left(-2qa\right)\right] = 0, \tag{50}$$

which leads to a bi-quadratic equation

$$2\left(\frac{\omega^2}{\Omega_p^2}\right)^2 - \left[1+\Xi\left(E_F,\Delta_\beta\right)\frac{2q}{\Omega_p^2}\right]\left(\frac{\omega^2}{\Omega_p^2}\right) + \Xi\left(E_F,\Delta_\beta\right)\frac{q}{\Omega_p^2}\left[1-\exp\left(-2qa\right)\right] = 0. \tag{51}$$

Eq. (51) gives rise to two solutions

$$\frac{4}{\Omega_p^2}\omega_{p,\pm}^2 = \left(1+\Xi\left(E_F,\Delta_\beta\right)\frac{2q}{\Omega_p^2}\right) \pm \sqrt{\left(1+\Xi\left(E_F,\Delta_\beta\right)\frac{2q}{\Omega_p^2}\right)^2 - \frac{8q\,\Xi\left(E_F,\Delta_\beta\right)}{\Omega_p^2}\left[1-\exp\left(-2qa\right)\right]}, \tag{52}$$

where $\pm$ terms correspond to in-phase and out-of-phase plasmon modes, respectively. Two hybrid plasmon modes in Eq. (52) become

$$\begin{aligned}\omega_{p,+}(q) &\simeq \frac{\Omega_p}{\sqrt{2}} + \frac{\Xi}{\sqrt{2}\Omega_p}q - \frac{\Xi\left(\Xi+4a\,\Omega_p^2\right)}{2\sqrt{2}\Omega_p^3}q^2 + \mathcal{O}\left(q^3\right),\\ \omega_{p,-}(q) &\simeq q\sqrt{2a\,\Xi} - \frac{\Xi\sqrt{2a\,\Xi}}{\Omega_p^2}q^2 + \mathcal{O}\left(q^3\right).\end{aligned} \tag{53}$$

In Eq. (53), both plasmon branches contain a linear $\sim q$ term, and $\omega_{p,+}(q)$ approaches a constant as $q \to 0$, i.e., an optical mode for plasmons. Two independent bandgaps, Δ_{SO} and Δ_z, together with doping density n, play a crucial role on shaping the plasmon dispersions, as well as the particle-hole mode damping regions. The outer boundaries of a particle-hole mode region specify an area within the q-ω plane in which the plasmon modes become damping free and are solely determined by $\Delta_<$, while the group velocity of plasmon mode depends on both $\Delta_<$ and $\Delta_>$. Since each bandgap could be experimentally tuned by applying a perpendicular electric field, we acquire a full control of both plasmon dispersions and their damping-free regions at the same time.

Numerical results for thermal plasmons in open system are presented in **Figure 9**. Similarly to what we have found for graphene and silicene, there are two plasmon branches, both of which depend linearly on q with a finite slope as $q \ll k_0$. The acoustic-plasmon branch starts from the origin, while the optical-plasmon branch from $\Omega_p/\sqrt{2}$. The dispersion of each branch also varies with parameter α (or $\phi = \tan^{-1}\alpha$), which is observed for the upper branch, as shown in (a) and (c) of **Figure 9**. In addition, we see a much smaller slope for the lower plasmon branch in **Figure 9(b)** and **(d)** due to enhanced Coulomb coupling with a reduced separation a. The finite-temperature upper plasmon branches in **Figure 9(e)** and **(f)** are shifted up greatly, as it is expected to be true for all finite-temperature plasmons, which is further accompanied by enhanced damping below the diagonal as seen in **Figure 6(c)**. Meanwhile, the lower plasmon branch seems much less affected by finite temperatures, as demonstrated by both upper and lower rows of **Figure 9** for different separations, except for enhanced damping in **Figure 9(f)** below the surface-plasmon energy $\hbar\Omega_p/\sqrt{2}$.

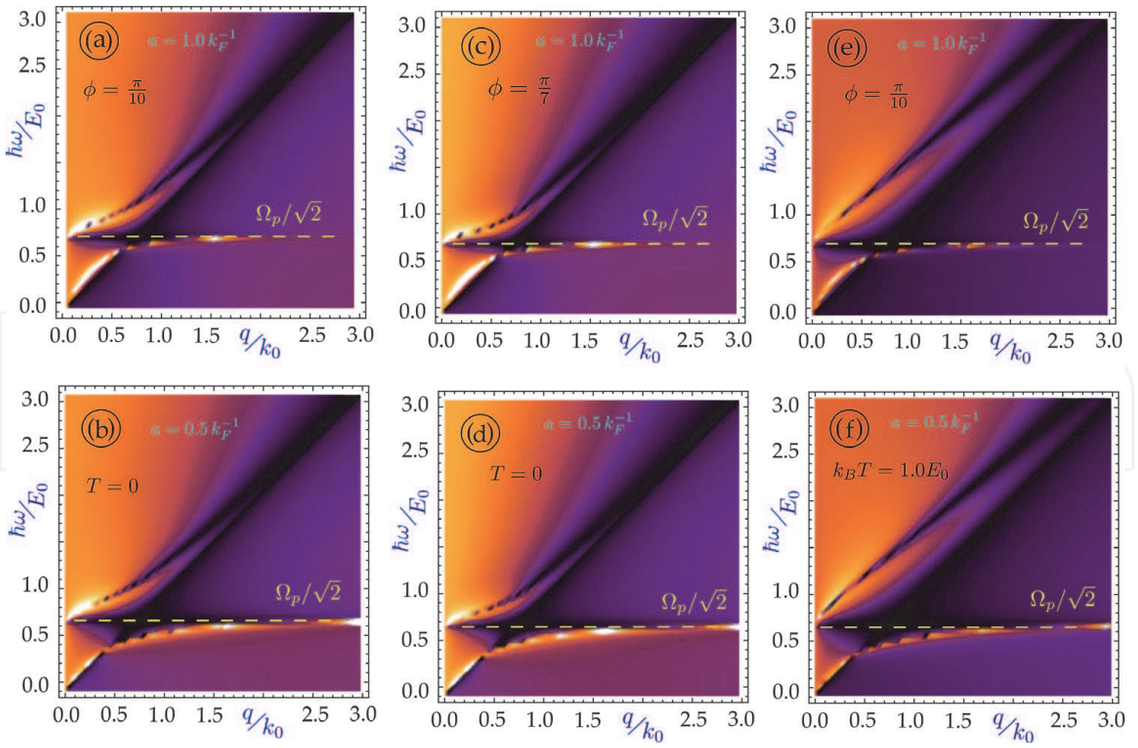


Figure 9.
Nonlocal hybridized plasmon dispersions for α-$\mathcal{T}_3$ layer coupled to a closely-located surface of a semi-infinite conductor. Panels (a)–(d) are for $\mathrm{T} = 0$, *while plots (e) and (f) for* $\mathrm{k_B T} = \mathrm{E_0}$. *All the upper-row plots correspond to the separation* $\mathrm{a} = 1.0\,\mathrm{k_F^{-1}}$, *and the lower-row ones to* $\mathrm{a} = 0.5\mathrm{k_F^{-1}}$. *Additionally, middle-column plots, (b) and (d), correspond to $\phi = \pi/7$, and all other columns to $\phi = \pi/10$.*

7. Summary and remarks

In conclusion, we have developed a general theory for finite-temperature polarization function, plasmon dispersions and their damping for all known innovation 2D Dirac-cone materials with various types of symmetries and bandgaps. We have also derived a set of explicit transcendental equations determining the chemical potential as a function of temperature, which serves as a key part in calculating finite-temperature polarization function through the so-called thermal convolution path. The selection of a particular path with a specific $\mu(T)$ could be employed for studying the temperature dependence of plasmon modes in each of the considered 2D materials. The fact that a chemical potential keeps its sign is true only for materials with symmetric energy bands of electrons and holes, but can cross the zero line for TMDC's with asymmetric electron and hole bands.

Using the calculated finite-temperature polarization function, we have further found the dispersions of hybrid plasmon-modes in various types of open systems including a 2D material coupled to a conducting substrate. The obtained plasmon dispersions in these 2D-layer systems are crucial for measuring spin-orbit interaction strength and dynamical screening to Coulomb interaction between electrons in 2D materials, as well as for designing novel surface-plasmon based multi-functional near-field opto-electronic devices.

We have generalized our developed theory for 2D materials further to most recently proposed α-$\mathcal{T}_3$ lattices, in which the characteristic parameter α is the ratio of hub-rim to hub-hub hopping coefficients and can vary from 0 to 1 continuously corresponding to different material properties. For α-$\mathcal{T}_3$ materials, we have obtained the hybrid plasmon modes for different α values at both zero and finite temperatures and demonstrated that the resulting hybridized plasmon dispersions

could be tuned sensitively by geometry phase, temperature, and separation between α-$\mathcal{T}_3$ layer and conducting surface. Such tunability has a profound influence on performance of α-$\mathcal{T}_3$ material based quantum electronic devices.

Acknowledgements

A.I. thanks Liubov Zhemchuzhna for helpful and fruitful discussions, and Drs. Armando Howard, Leon Johnson and Ms. Beverly Tarver for proofreading the manuscript and providing very useful suggestions on the style and language. G.G. would like to acknowledge the financial support from the Air Force Research Laboratory (AFRL) through grant FA9453-18-1-0100 and award FA2386-18-1-0120. D.H. thanks the supports from the Laboratory University Collaboration Initiative (LUCI) program and from the Air Force Office of Scientific Research (AFOSR).

Conflict of interest

All the authors declare that they have no conflict of interest.

Author details

Andrii Iurov[1*], Godfrey Gumbs[2,3] and Danhong Huang[4]

1 Department of Physics and Computer Science, Medgar Evers College of the City University of New York, Brooklyn, NY, USA

2 Department of Physics and Astronomy, Hunter College of the City University of New York, NY, USA

3 Donostia International Physics Center (DIPC), San Sebastian, Basque Country, Spain

4 Air Force Research Laboratory, Space Vehicles Directorate, Kirtland Air Force Base, NM, USA

*Address all correspondence to: aiurov@mec.cuny.edu; theorist.physics@gmail.com

IntechOpen

© 2020 The Author(s). Licensee IntechOpen. This chapter is distributed under the terms of the Creative Commons Attribution License (http://creativecommons.org/licenses/by/3.0), which permits unrestricted use, distribution, and reproduction in any medium, provided the original work is properly cited.

References

[1] Novoselov K, Geim AK, Morozov S, Jiang D, Katsnelson M, Grigorieva I, et al. Two-dimensional gas of massless Dirac fermions in graphene. Nature. 2005;**438**:197

[2] Geim AK, Novoselov KS. The rise of graphene. Nature Materials. 2007;**6**:183

[3] Neto AC, Guinea F, Peres N, Novoselov KS, Geim AK. The electronic properties of grapheme. Reviews of Modern Physics. 2009;**81**:109

[4] Grigorenko A, Polini M, Novoselov K. Graphene plasmonics. Nature Photonics. 2012;**6**:749

[5] Agarwal A, Vitiello MS, Viti L, Cupolillo A, Politano A. Plasmonics with two-dimensional semiconductors: From basic research to technological applications. Nanoscale. 2018;**10**:8938

[6] Katsnelson M, Novoselov K, Geim A. Chiral tunneling and the Klein paradox in graphene Nature Physics. 2006;**2**:620

[7] Low T, Roldán R, Wang H, Xia F, Avouris P, Moreno LM, et al. Plasmons and screening in monolayer and multilayer black phosphorus. Physical Review Letters. 2014;**113**:106802

[8] Soleimanikahnoj S, Knezevic I. Tunable electronic properties of multilayer phosphorene and its nanoribbons. Journal of Computational Electronics. 2017;**16**:568

[9] Koppens FH, Chang DE, Garcia de Abajo FJ. Graphene plasmonics: A platform for strong light-matter interactions. Nano Letters. 2011;**11**:3370

[10] Garcia de Abajo FJ. Graphene plasmonics: Challenges and opportunities. ACS Photonics. 2014; **1**:135

[11] Politano A, Chiarello G. Plasmon modes in graphene: Status and prospect. Nanoscale. 2014;**6**:10927

[12] Politano A, Radović I, Borka D, Mišković Z, Yu H, Farias D, et al. Dispersion and damping of the interband π plasmon in graphene grown on Cu (111) foils. Carbon. 2017;**114**:70

[13] Politano A, Chiarello G. Quenching of plasmons modes in air-exposed graphene-Ru contacts for plasmonic devices. Applied Physics Letters. 2013; **102**:201608

[14] Politano A, Marino AR, Chiarello G. Effects of a humid environment on the sheet plasmon resonance in epitaxial grapheme. Physical Review B. 2012;**86**: 085420

[15] Iurov A, Huang D, Gumbs G, Pan W, Maradudin A. Effects of optical polarization on hybridization of radiative and evanescent field modes. Physical Review B. 2017;**96**:081408

[16] Das Sarma S, Li Q. Intrinsic plasmons in two-dimensional Dirac materials. Physical Review B. 2013;**87**: 235418

[17] Hwang EH, Das Sarma S. Screening-induced temperature-dependent transport in two-dimensional graphene. Physical Review B. 2009;**79**:165404

[18] Iurov A, Gumbs G, Huang D, Balakrishnan G. Thermal plasmons controlled by different thermal-convolution paths in tunable extrinsic Dirac structures. Physical Review B. 2017;**96**:245403

[19] Tabert CJ, Nicol EJ. Dynamical polarization function, plasmons, and screening in silicene and other buckled honeycomb lattices. Physical Review B. 2014;**89**:195410

[20] Tabert CJ, Nicol EJ. AC/DC spin and valley Hall effects in silicene and germanene. Physical Review B. 2013;**87**: 235426

[21] Kane CL, Mele EJ. Quantum spin Hall effect in grapheme. Physical Review Letters. 2005;**95**:226801

[22] Ezawa M. A topological insulator and helical zero mode in silicene under an inhomogeneous electric field. New Journal of Physics. 2012;**14**:033003

[23] Ezawa M. Valley-polarized metals and quantum anomalous Hall effect in silicone. Physical Review Letters. 2012; **109**:055502

[24] Liu C-C, Feng W, Yao Y. Quantum spin Hall effect in silicene and two-dimensional germanium. Physical Review Letters. 2011;**107**:076802

[25] Iurov A, Gumbs G, Huang D, Zhemchuzhna L. Controlling plasmon modes and damping in buckled two-dimensional material open systems. Journal of Applied Physics. 2017;**121**: 084306

[26] Chang H-R, Zhou J, Zhang H, Yao Y. Probing the topological phase transition via density oscillations in silicene and germanene. Physical Review B. 2014;**89**: 201411

[27] d'Acapito F, Torrengo S, Xenogiannopoulou E, Tsipas P, Velasco JM, Tsoutsou D, et al. Evidence for Germanene growth on epitaxial hexagonal (h)-AlN on Ag(111). Journal of Physics: Condensed Matter. 2016;**28**: 045002

[28] Walhout C, Acun A, Zhang L, Ezawa M, Zandvliet H. Scanning tunneling spectroscopy study of the Dirac spectrum of germanene. Journal of Physics: Condensed Matter. 2016;**28**: 284006

[29] Derivaz M, Dentel D, Stephan R, Hanf M-C, Mehdaoui A, Sonnet P, et al. Continuous germanene layer on Al (111). Nano Letters. 2015;**15**:2510

[30] Bampoulis P, Zhang L, Safaei A, Van Gastel R, Poelsema B, Zandvliet HJW. Germanene termination of Ge_2Pt crystals on Ge(110). Journal of Physics: Condensed Matter. 2014;**26**:442001

[31] Acun A, Zhang L, Bampoulis P, Farmanbar M, van Houselt A, Rudenko A, et al. Germanene: The germanium analogue of grapheme. Journal of Physics: Condensed Matter. 2015;**27**: 443002

[32] Zhang L, Bampoulis P, van Houselt A, Zandvliet H. Two-dimensional Dirac signature of germanene. Applied Physics Letters. 2015;**107**:111605

[33] Pyatkovskiy P. Dynamical polarization, screening, and plasmons in gapped graphene. Journal of Physics: Condensed Matter. 2008;**21**:025506

[34] Maldague PF. Many-body corrections to the polarizability of the two-dimensional electron gas. Surface Science. 1978;**73**:296

[35] Iurov A, Gumbs G, Huang D, Silkin V. Temperature-dependent plasmons and their damping rates for graphene with a finite energy bandgap. arXiv preprint arXiv:1504.04552. 2015

[36] Iurov A, Gumbs G, Huang D, Silkin V. Plasmon dissipation in gapped graphene open systems at finite temperature. Physical Review B. 2016; **93**:035404

[37] Falkovsky L, Varlamov A. Space-time dispersion of graphene conductivity. The European Physical Journal B. 2007;**56**:281

[38] Gusynin V, Sharapov S. Transport of Dirac quasiparticles in graphene: Hall

and optical conductivities. Physical Review B. 2006;**73**:245411

[39] Singh A, Bolotin KI, Ghosh S, Agarwal A. Nonlinear optical conductivity of a generic two-band system with application to doped and gapped grapheme. Physical Review B. 2017;**95**:155421

[40] Falkovsky L, Pershoguba S. Optical far-infrared properties of a graphene monolayer and multilayer. Physical Review B. 2007;**76**:153410

[41] Iurov A, Gumbs G, Huang D. Temperature-and frequency-dependent optical and transport conductivities in doped buckled honeycomb lattices. Physical Review B. 2018;**98**:075414

[42] Iurov A, Gumbs G, Huang D. Temperature-dependent collective effects for silicene and germanene. Journal of Physics: Condensed Matter. 2017;**29**:135602

[43] Tsaran VY, Kavokin A, Sharapov S, Varlamov A, Gusynin V. Entropy spikes as a signature of Lifshitz transitions in the Dirac materials. Scientific Reports. 2017;**7**:10271

[44] Gorbar EV, Gusynin VP, Miransky VA, Shovkovy IA. Magnetic field driven metal-insulator phase transition in planar systems. Physical Review B. 2002;**66**:045108

[45] Raoux A, Morigi M, Fuchs J-N, Piéchon F, Montambaux G. From dia- to paramagnetic orbital susceptibility of massless fermions. Physical Review Letters. 2014;**112**:026402

[46] Iurov A, Gumbs G, Huang D. Peculiar electronic states, symmetries, and Berry phases in irradiated materials. Physical Review B. 2019;**99**:205135

[47] Oriekhov D, Gorbar E, Gusynin V. Electronic states of pseudospin-1 fermions in dice lattice ribbon. Low Temperature Physics. 2018;**44**:1313

[48] Dey B, Ghosh TK. Photoinduced valley and electron-hole symmetry breaking in α-T_3 lattice: The role of a variable Berry phase. Physical Review B. 2018;**98**:075422

[49] Gorbar E, Gusynin V, Oriekhov D. Electron states for gapped pseudospin-1 fermions in the field of a charged impurity. Physical Review B. 2019;**99**: 155124

[50] Malcolm J, Nicol E. Frequency-dependent polarizability, plasmons, and screening in the two-dimensional pseudospin-1 dice lattice. Physical Review B. 2016;**93**:165433

[51] Iurov A, Zhemchuzhna L, Dahal D, Gumbs G, Huang D. Quantum-statistical theory for laser-tuned transport and optical conductivities of dressed electrons in α-T3 materials. Physical Review B. arXiv preprint arXiv: 1905.01703. 2019 [accepted for publication]

[52] Huang D, Iurov A, Xu H-Y, Lai Y-C, Gumbs G. Interplay of Lorentz-Berry forces in position-momentum spaces for valley-dependent impurity scattering in lattices. Physical Review B. 2019;**99**: 245412

[53] Horing NJM. Coupling of graphene and surface plasmons. Physical Review B. 2009;**80**:193401

[54] Gumbs G, Iurov A, Horing N. Nonlocal plasma spectrum of graphene interacting with a thick conductor. Physical Review B. 2015;**91**:235416

[55] Horing NJM. Aspects of the theory of grapheme. Philosophical Transactions of the Royal Society of London A: Mathematical, Physical and Engineering Sciences. 2010;**368**:5525

[56] Horing NJM, Kamen E, Cui H-L. Inverse dielectric function of a bounded solid-state plasma. Physical Review B. 1985;**32**:2184

[57] Horing N, Iurov A, Gumbs G, Politano A, Chiarello G. Recent progress on nonlocal graphene/surface plasmons. In: Low-dimensional and Nanostructured Materials and Devices. 2016. Available from: https://link.springer.com/chapter/10.1007/978-3-319-25340-4_9

[58] Kramberger C, Hambach R, Giorgetti C, Rümmeli M, Knupfer M, Fink J, et al. Linear plasmon dispersion in single-wall carbon nanotubes and the collective excitation spectrum of grapheme. Physical Review Letters. 2008;**100**:196803

IntechOpen